Received: 21 April 2021 | Revised: 14 December 2021 | Accepted: 22 January 2022

DOI: 10.1002/rob.22065

RESEARCH ARTICLE

WILEY

Characteristics of optical flow from aerial thermal imaging, "thermal flow"

Tran Xuan Bach Nguyen[1] | Kent Rosser[2] | Asanka Perera[1] | Philip Moss[3] | Sam Teague[1] | Javaan Chahl[2]

[1]Department of STEM, University of South Australia, Adelaide, South Australia, Australia

[2]Defence Science and Technology Group, University of South Australia, Adelaide, South Australia, Australia

[3]Defence Science and Technology Group, Edinburgh, South Australia, Australia

Correspondence
Tran Xuan Bach Nguyen, Department of STEM, University of South Australia, SCT2-07, Mawson Lake, SA 5095, Australia.
Email: nguty219@mymail.unisa.edu.au

Funding information
Australian government Research Training Program (RTP) scholarship

Abstract

This study explores the utility of optical flow calculated from thermal imaging cameras, "thermal flow," mounted on an aircraft for localization in day and night conditions. Our sensor implementation utilizes a long wave infrared (LWIR) micro sensor to capture sequences of thermal images and an on-board computer to compute an optical flow estimate. We compared the performance of optical flow from the LWIR camera with the output of visible spectrum optical flow sensor. Flights were conducted spanning a 24 h window to explore how thermal flow performs relative to optical flow as the ground heats and cools. Agreement between optical and thermal flow was found during daylight when both sensors were functional. Additionally, thermal flow results were reliable in the middle of the day through to late evening, gradually degrading until shortly after sunrise.

KEYWORDS
aircraft, LWIR, navigation, optical flow, thermal imaging, UAV

1 | INTRODUCTION

The use of unmanned aerial vehicles (UAVs) has been increasing rapidly due to decreasing cost and increasing maturity. Some dangerous and laborious aerial jobs are being replaced by drones and new drone applications are being discovered. Drones perform routine tasks such as inspecting vast cropped areas (Jordan et al., 2017), inspecting and finding faults on hundreds of kilometers of power line (Fernandes, 1989; Sato & Anezaki, 2017; Varghese et al., 2017), in search and rescue missions (Al-Naji et al., 2018; Perera et al., 2019) and being sent to inaccessible places to deliver first aid to patients (Al-Al-Naji, Gibson, et al., 2017; Al-Al-Naji, Perera, et al., 2017). Armed UAVs have participated in armed conflict with great success. Billions of dollars are being invested in drone technologies to refine and extend their capabilities in all applications.

However, fundamental work remains to be done before drones can operate in all environments. Currently, many small UAVs navigate with the Global Positioning Systems (GPS) alone, with virtually no period of autonomy possible from their inexpensive Inertial Measurement Unit (IMU) and also have no environment or obstacle sensing capability (Lu et al., 2018). However, this limits the use of UAVs in many scenarios such as indoors, urban areas, underground or very close to the ground.

Optical flow is defined as the apparent motion of image intensities or brightness patterns across two consecutive frames (Horn & Schunck, 1981). Optical flow for navigation and flight control is a solution inspired from nature particularly flying insects that are acutely sensitive to visual motion (Srinivasan et al., 1999). Honeybees rely on optical flow for grazing landings (Chahl et al., 2004; Srinivasan, Zhang, Altwein, et al., 2000), obstacle avoidance (Srinivasan, 2010) and flight speed

regulation (Esch & Burns, 1996). Computer vision using images from UAVs can be problematic because of the number of variables involved. For instance, poor camera or aircraft stability can cause blurry images (Cruz & Bernardino, 2016), smaller objects observed from high altitude means fewer pixels to work with and there is the need to manage different views and angles, which comes from the high number of degrees of freedom of motion of UAVs (Gan & Sukkarieh, 2011; Perera et al., 2018). The quality of captured images and the optical flow patterns they capture are influenced by roll, pitch and yaw movement of the UAV.

Many optical flow algorithms have been developed by computer scientists and biologists. Some examples include the Horn and Shunck technique (Horn & Schunck, 1981), the Farneback algorithm (Farnebäck, 2003), gradient-based methods such as Lucas–Kanade (LK) (Lucas & Kanade, 1981), energy and frequency-based methods (Beauchemin & Barron, 1995), correlation and block matching methods (Dabov et al., 2006) and the image interpolation technique (Srinivasan, 1994). These algorithms can produce accurate optical flow fields when compared with subpixel accuracy ground truth standards (Baker et al., 2011). Generally, dense optical flow algorithms are known for being computationally demanding, which has made them less desirable for real-time applications in the past. The LK algorithm is one of the more common robotics techniques due to its modest computational requirement, while still producing reliable flow fields.

2 | OPTICAL FLOW FOR NAVIGATION

Optical flow can be used for active navigation such as frontal obstacle avoidance and altitude control in buildings (Miller et al., 2018). Optical flow can also be used passively to collect the current operating state of the aircraft such as pitch and roll rates (Chahl et al., 2005; Honegger et al., 2013), descent angles (Barrows et al., 2002), direction of travel or lateral drift (Franz et al., 2004; Garratt & Chahl, 2003; Rosser & Chahl, 2019), to perform altitude control or automatic landing (Chahl et al. 2004; Srinivasan, Zhang, Chahl, et al., 2000).

Camus (1995) proposed a method utilizing optical flow in real time to calculate time to contact or time to collision for a robot. Zingg et al. (2010) used a fish-eye camera with 190° field of view mounted facing the direction of travel to map the optical flow to estimate a depth map across the visual field for collision avoidance. By combining this field with IMU readings to compensate for rotational effects, the MAV could stay in the center of an indoor corridor.

Dusha et al. (2007) presented the idea of estimating attitude for fixed wing aircraft by combining optical flow and horizon detection. The algorithm was based on detecting lines in the image that should correspond to the horizon. A camera was mounted in front of the aircraft to capture images, then several image processing techniques were applied in each color channel for edge detection. By computing optical flow from the horizon, the attitude of the aircraft could be estimated. During testing, their algorithm could detect the horizon line correctly 90% of the time.

Zufferey and Floreano (2005) used an optical flow sensor pointing downward from a UAV to maintain altitude. The optical flow measurement was maintained constant, which kept the vehicle at a constant height. A similar idea was also presented by Chahl and Mizutani (2006) to fly at fixed altitude above the ground by maintaining optical flow at a constant value leading to automatic reduction of horizontal velocity when height decreased. Thus, if the descent speed was proportionate to the forward speed, the descent angle remained constant.

Srinivasan (1994) proposed a landing technique inspired by insect behavior. Insects use optical flow to aid in navigation. This technique can ensure a smooth landing without explicit knowledge of the flight speed or altitude. The feasibility of this strategy was tested by implementation on a robot gantry.

Rosser and Chahl (2019) used the angle of optical flow from a downward looking camera on a fixed wing aircraft flying straight segments to reduce lateral drift caused by wind. The method combines the kinematics of fixed wing aircraft, the optical flow field and a magnetic compass to create a bio-inspired optomotor response inspired by insect behavior (Chahl & Mizutani, 2006). The authors tested their system in three distinctive environments showing clear reductions in drift over long distances.

These studies have shown the potential of using optical flow with optical wavelength camera sensors to achieve various tasks for navigation. However, most of the works must be done during daytime or environments with abundant light. To compute optical flow at night or in a dark environment, a thermal sensor might be used.

Some early studies have explored the use of a LWIR sensor in agriculture to monitor crops, manage water, or to aid navigation at night. The use of high resolution thermal cameras, installed on UAVs, were used outdoors for a long period of time for detecting and sensing crops commercially were described in Gonzalez-Dugo et al. (2013), Meron et al. (2013), Alchanatis et al. (2010). Based on the difference in temperature of the trees and the air, the growth rate of five fruit species can be easily monitored on a very large scale. Furthermore, the data can further be used in water management for the plantation for maximize production.

Early thermal LWIR sensors suffered from size and weight constraints which limited their use for airborne application. Furthermore, automatic gain control (AGC) was provided to maximize dynamic range due to lower bit resolution. However, it severely changes image pixel values and contrast when hot or cold objects suddenly enter a scene.

Brunner et al. (2013) combined both visual and thermal sensor data with simultaneous localization and mapping (SLAM) to enhance its reliability by detecting and rejecting unusable areas from the image.

Khattak et al. (2018) utilized recent developments in reduction of both weight, size and resolution of LWIR sensors for aircraft navigation. In Khattak et al. (2020), they designed fiducial markers that could be sensed by LWIR sensor for navigating an indoor workshop scene. In Khattak et al. (2019), they developed a thermal-inertial odometry estimation framework for thermal sensors with AGC disabled, which showed the LWIR sensor could be used in many dark scenarios indoors, in urban areas and in underground mine environments.

Rosser et al. (2021) explored the use of low cost, low resolution LWIR sensor mounted on a fixed wing aircraft. The study shows optical flow computed from thermal frames works comparably well during the day and continue to work at night.

These studies have shown that LWIR sensors have potential as the input to visual navigation algorithms at night. However, all of these studies were conducted during a short span of time, which did not evaluate the performance of the sensor over a longer time span into the late night when the environment is cooling down, or early morning when the environment is heating up.

3 | CONTRIBUTION

The use of optical flow for a LWIR sensor had been demonstrated to work with ground vehicle by Borges and Vidas (2016). Furthermore, Delaune et al. (2019) studied the feasibility of using a LWIR sensor for aerial applications. However, those studies relied on high resolution LWIR sensor at 640 × 512 pixels or above. Furthermore, the last study only conducted four tests at before and after sunset and sunrise, which is somewhat insufficient. Furthermore, various Feature Detectors had been evaluated by Mouats et al. (2018) on a Intel(R) Core(TM) i7- 3770 CPU at 3.40 GHz machine. However, due to high computational cost, these algorithms cannot be used with our representative low cost, low power on-board computer.

The study continues our work in Rosser et al. (2021) to analyze the performance of thermal flow over 24 h. In this study, we have explored the viability of using a low resolution at 160 × 120 pixels, 8–12 micron thermal camera as a sensor for optical flow-based aerial navigation and odometry techniques. Additionally, we also propose a down sampling technique to rescale fourteen bit to eight bit data to be compatible with OpenCV library. Our system was implemented so as to mimic the input and output of the popular, optical wavelength, PX4Flow sensor and processor Honegger et al. (2013) at the protocol level. With a view to answering the question: Can a low resolution thermal camera provide useful imagery for navigation of the ground over day and night? Our experiments were run over a 24 h period to test how the daily cycle of heating and cooling might affect a practical drone implementation. Our contribution is significant because:

- There is currently a gap in investigation of thermal imaging over longer time spans. Our work further enhances the field by investigating the reliability of thermal imaging over a full hot and cold cycles over 24 h.
- We proposed a new scaling technique that performs reliably that more fully overcomes the AGC issues with eight bit images for feature tracking algorithms.
- We show the effect of running optical flow algorithms on real thermal data from aerial systems across the day night cycle. This should improve understanding of what real-world challenges thermal computer vision-based robotic behavior will face.

The paper is organized in 10 sections. Section 4 reviews the LK optical algorithm, and its implementation in OpenCV. Section 5 describes the system implementation including hardware and software architectures. Section 6 considers our assessment methodology including flying platform, flight path and conditions of the site. Sections 7 and 8 reports and analyses collected data from the flight and their performance. Section 9 concludes the lesson learn and plans for future research. Additionally, Supporting Information can be found in the appendix in Section 10.

4 | LK ALGORITHM

The LK algorithm was proposed in 1981 (Lucas & Kanade, 1981), as an attempt to produce a dense optical flow solution. However, the algorithm relied on local information derived from some small windows surrounding each point of interest, so it has been used subsequently as a sparse technique, which tracks a limited number of high-quality interest points from one frame to the next.

The technique relies on three assumptions (Horn & Schunck, 1981; Lucas & Kanade, 1981):

1. Brightness constancy: The pixel intensities of an object do not differ between two consecutive frames.
2. Small movements: The displacement between two consecutive frames must be less than 1 pixel.
3. Spatial coherence: The neighboring pixels move together and have the same motion.

Considering the first assumption, brightness constancy, which is the requirement that apparently moving pixels look the same between frames. Consider pixel $I(x(t), y, t)$. It displaces (u, v) pixels in the next frame. We have

$$f(x) \equiv I(x, y) = I(x + u, y + v). \tag{1}$$

Since our tracked pixel intensity does not change over time:

$$\frac{\partial f(x)}{\partial t} = 0. \tag{2}$$

This constraint should be met by a thermal image of a natural surface when the scale between a pair of images is constant. We implemented a technique to convert from 14 bit radiometric images pairs to have the same scale based on high and low intensity pixels in both. The technique will be described in Section 5.2.2.

The second assumption, small movements, means that pixel motion is small between frames. Applying the Taylor series approximation to the right-hand side then simplify,

$$\begin{aligned} I(x + u, y + v) &= I(x, y) + \frac{\partial I}{\partial x}u + \frac{\partial I}{\partial y}v + HigherOrderTerms \\ &\Rightarrow \approx I(x, y) + \frac{\partial I}{\partial x}u + \frac{\partial I}{\partial y}v. \end{aligned} \tag{3}$$

From Equations (1) and (3), we get the *optical flow* equation:

$$I_x u + I_y v + I_t = 0, \tag{4}$$

where I_t is the time derivative of the image at pixel (x, y).

Equation (4) cannot be solved with one equation as there are two unknowns, u and v, per pixel. This is a geometrical constraint for

drone imagery, where speed of the aircraft and height above ground will define the amount of movement. The thermal image can meet this requirement for optical flow as well.

Optical flow estimation can suffer from the *aperture problem*, which happens when motion of a featureless bar or single direction gradient is measured with a small aperture or window. That is when motion is detected only perpendicular to the edge so all components of motion may not be detected.

To solve this problem, the LK algorithm uses the assumption that the motion field is smooth, which means nearby pixels have similar motion. To solve Equation (4) for a central pixel, the surrounding pixels are utilized to set up a system of equations. For example, if we choose a 5×5 window, that gives us 25 equations per pixel.

$$\begin{bmatrix} I_x(P_1) & I_y(P_1) \\ I_x(P_2) & I_y(P_2) \\ \vdots & \vdots \\ I_x(P_{25}) & I_y(P_{25}) \end{bmatrix} \begin{bmatrix} u \\ v \end{bmatrix} = - \begin{bmatrix} I_t(P_1) \\ I_t(P_2) \\ \vdots \\ I_t(P_{25}) \end{bmatrix}, \tag{5}$$

where

$$A = \begin{bmatrix} I_x(P_1) & I_y(P_1) \\ I_x(P_2) & I_y(P_2) \\ \vdots & \vdots \\ I_x(P_{25}) & I_y(P_{25}) \end{bmatrix},$$

$$d = \begin{bmatrix} u \\ v \end{bmatrix},$$

$$b = \begin{bmatrix} I_t(P_1) \\ I_t(P_2) \\ \vdots \\ I_t(P_{25}) \end{bmatrix}.$$

Equation (5) can be solved with minimum least squares solution where we minimize $\|Ad - b\|^2$ is solved as

$$(A^T A)d = A^T b. \tag{6}$$

From Equations (5) and (6), then the solution for (u, v) can be expressed as

$$\begin{bmatrix} u \\ v \end{bmatrix} = (A^T A)^{-1} A^T b. \tag{7}$$

The biggest disadvantage of the LK technique is that local search windows cannot be used to measure large motions. This happens when the interest points move outside of a window due to large motion and become impossible to detect. For large displacements, the pyramidal variation of the LK algorithm was developed (Bouguet, 2001). This augmentation of the algorithm tracks from the highest level of an oversampled image pyramid to lower levels enabling it to track faster movement. The LK algorithm is implemented in OpenCV (Bradski, 2000) and is widely used by researchers and enthusiasts for optical flow applications.

We used the Pyramid LK algorithm built into the OpenCV library as our implementation for optical flow estimation. The LK algorithm in OpenCV was selected due to its capability for real-time operation and because its ubiquity focused our work on the findings from the data rather than the algorithm.

5 | SYSTEM IMPLEMENTATION

In this section, we present our system implementation including the hardware and software architecture. In the hardware implementation, the overview of system's blocks, and the components including on-board computer, sensor, battery will be presented. Furthermore, our system's firmware, the scaling techniques will be also discussed and analyzed.

5.1 | Hardware implementation

Figure 1 shows a block diagram of the hardware implementation of the payload. The system is powered by a Li-Po battery through a UBEC Voltage regular to ensure voltage and current are maintained constantly during high and low loads. Inside the payload, the on-board computer powers the two PixHawks, while receiving data via Serial interface "TELEM 2" interface. Simultaneously, the on-board computer also receives constant streams of thermal images from the Lepton3 via USB interface.

Figure 2 our constructed payload in the housing frame, with components are labeled in red.

5.1.1 | Thermal sensor

The FLIR Lepton3 is a LWIR sensor with 160×120 resolution. The sensor has a 56° field of view, can output images at 8.7 Hz (FLIR Corp., 2018). In our previous work (Rosser et al., 2021), the Lepton3 was shown to be adequate for navigation tasks with small angular movements without needing further calibration. The sensor comes with a built-in shutter for Flat Field Correction (FFC) for stationary usage. This is an offset calibration executed at power up, when changing temperature and periodically during operation (every 3 min) (FLIR Corp., 2018). FFC compensates for certain bias errors that develop during camera operation. The camera updates the offset correction coefficients, resulting in a more uniform image after the process is completed. For other scenarios in which there is scene movement, the Lepton is capable of automatically adjusting for drift effects with internal calibration algorithms. Since the system is mounted on a constantly moving aircraft, which makes FFC not useful. Hence, it is essential to disable FFC to maintain a constant output images.

5.1.2 | Interfacing with the lepton

The PureThermal 2 board can provides access to the fourteen bit radiometric pixel data. We modified the PureThermal 2 firmware to

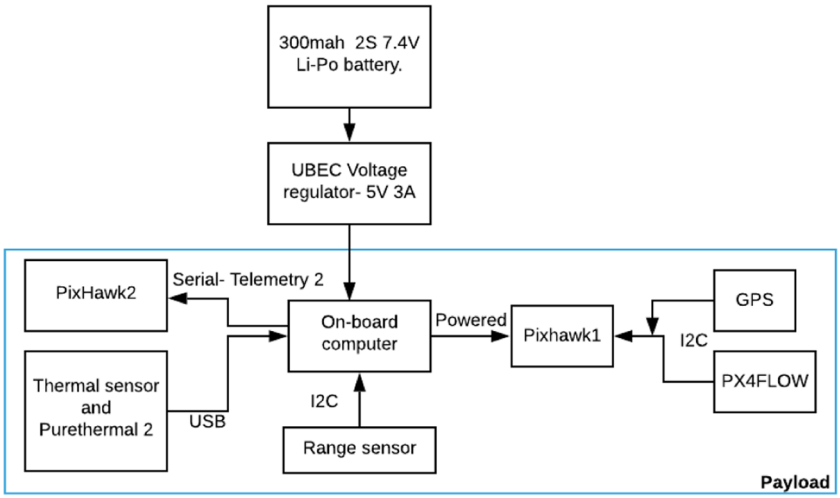

FIGURE 1 Hardware implementation block diagrams of the system

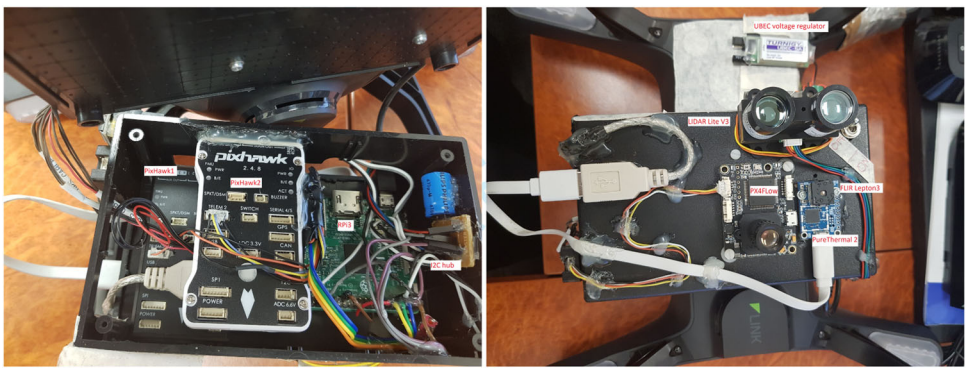

FIGURE 2 Inside (on the left) and outside (on the right) of the payload. The inside contains PixHawk, the RPi3, and connections. LIDAR, the PX4Flow and the FLIR Lepton3 are on the outside of the payload, facing downward

disable the FFC process and send fourteen bit raw thermal frames via USB under HY16 mode. The saved raw frames were used for post analysis.

5.1.3 | Range sensor

A LIDAR lite v3 was used in this study due to its light weight of only 22 grams, low power consumption, long range measurement capability and an I2C interface (Garmin, 2016). Its size is 40 × 48 × 20 mm (H × W ×D), which made it ideal for this weight constrained situation. The purpose of the LIDAR is for post-flight altitude verification.

5.1.4 | On-board computer

All computation was done on-board with a Raspberry Pi 3 model B+ (RPi). The RPi downloads thermal frames from the PureThermal board via a USB interface, measures distance from the LIDAR lite v3 and samples the real-time clock via I2C. The optical flow MAVLINK packet, "OPTICAL_FLOW_RAD" was then sent to the onboard PixHawk via Serial interface "TELEM 2."

5.2 | Software implementation

Figure 3 shows the structure the "thermal flow sensor firmware." All of the computing tasks were done on the RPi, and written in python. The program starts with the script requesting raw thermal data under HY16 mode from the PureThermal board. The raw frames were saved, while simultaneously being converting to eight bit data with a common scale. The two processed eight bit frame were then processed with Shi-Tomasi and the LK algorithms in the OpenCV library to determine optical flow: flow_x, flow_y. The ground distance data was received from the LIDAR. After that, the optical flow and the ground distance information were sent to PixHawk2 via "OPTICALFLOWRAD" MAVLINK package to be saved in Ulog format. PixHawk1 also receives the PX4Flow and GPS data in Ulog format.

5.2.1 | Optical flow with radiometric imagery assumptions

Most optical flow algorithms are based on assumptions of brightness constancy across two frames as described in Section 4. However, most available thermal sensors apply AGC by default, which means

FIGURE 3 Software algorithm block diagram

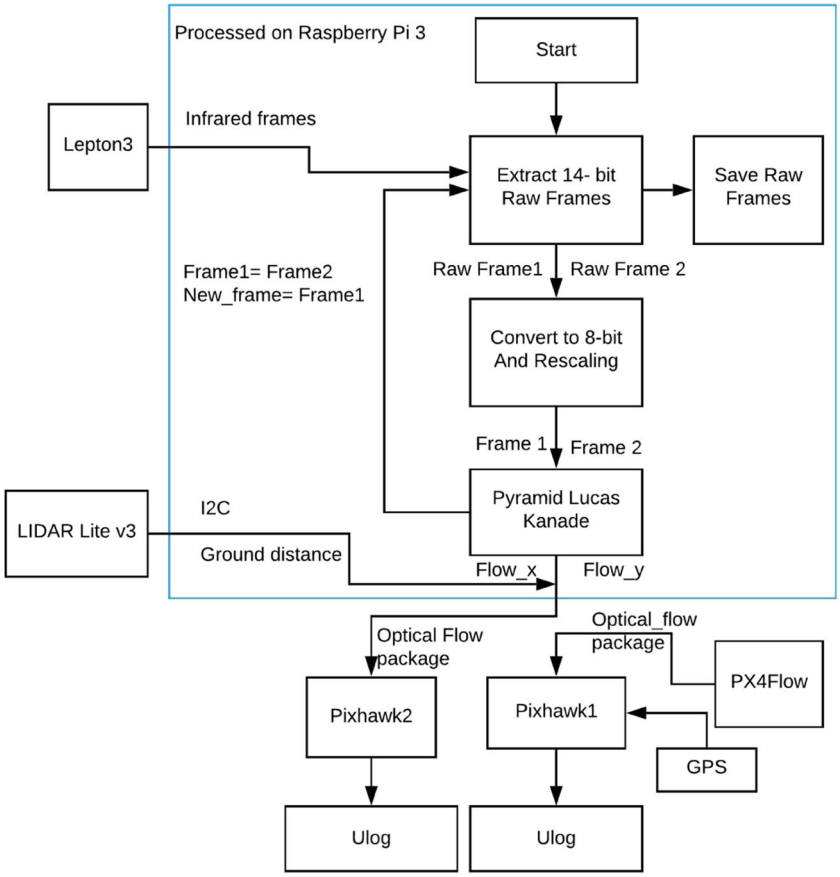

FIGURE 4 Change of contrast caused by AGC when a hot object moves out a scene. (a) Frame 1 and (b)Frame 2

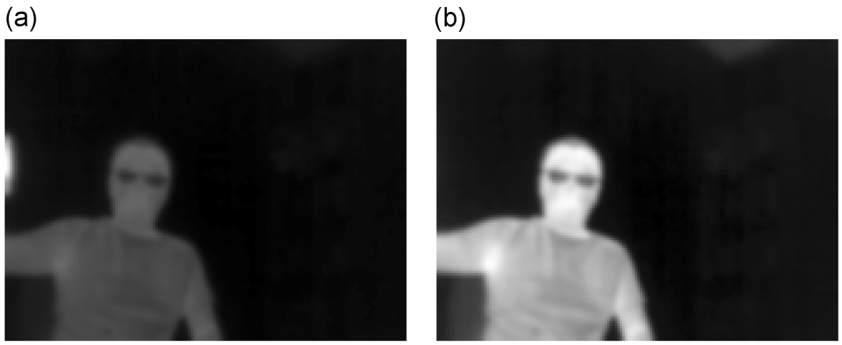

the AGC re-scales the image based on the hottest and coolest pixel values in a frame. Figure 4 shows a pair of images captured consecutively by the sensor, which shows the inconstancy of the brightness between them.

AGC is essential for display purposes, allowing an operator to visually identify the hottest/coldest spot from a display device. AGC makes optical flow estimation impossible between two frames since the brightness of a second frame might change if one hotter or cooler pixel comes into the field. Hence, it was essential to disable the AGC function and find a common scale for each pair of images. An example can be found in Figure 7, which achieves brightness constancy for pixels representing the same parts of the scene in consecutive frames.

Figure 4 shows one example of the effect of the AGC on thermal brightness constancy. The eight bit images, image1 and image2, were captured indoors, with a hot cup moving out of the second frame. The result shows that the range of pixel intensities in the two images are vastly different, leading to the AGC ensuring that the brightness is not consistent between them, which violates the first condition for optical flow estimation, which is brightness constancy.

There are several proposed techniques to overcome this AGC problem. Mouats et al. (2015) attempted to reduce the response time of AGC so the brightness would not change too drastically for feature tracking algorithms. However, this proposal did not completely solve the problem, although it did reduce the effect. Furthermore, this technique proved to be problematic with algorithms that rely on spatiotemporal gradient information, of which the LK is one. Hence, this technique could not be used in this study.

A second approach is to set the range of the AGC from Papachristos et al. (2018), but it requires prior knowledge of the environment, which is not possible in this study. Another approach is to simply skip the trouble converting AGC process, utilizing on the full radiometric 14 bit data (Khattak et al., 2020). Nevertheless, since the LK and the Shi-Tomasi algorithms in OpenCV only accept eight bit input images, this solution is not viable.

In the next section, we proposed a technique to rescale two fourteen bit data to two equivalent eight bit frames with the same scaling factor.

5.2.2 | Scaling radiometric pairs

The intensity scale between a pair of images must be the same. This can be achieved while converting from fourteen bit to eight bit images suitable for OpenCV. From two raw 14 bit images captured by the Lepton3, which are *Image1* and *Image2*.

Figure 5 shows our algorithm converting from a pair of fourteen bit thermal images to eight bit with the same scaling factor, based on the minimum and maximum pixel values from each fourteen bit raw image.

Figure 6 shows a rescaled version of our previous affect of AGC in Figure 4. The results show that brightness does not change between two frames visually. However, there are some small artifacts in the images with minimal impact on the overall image data.

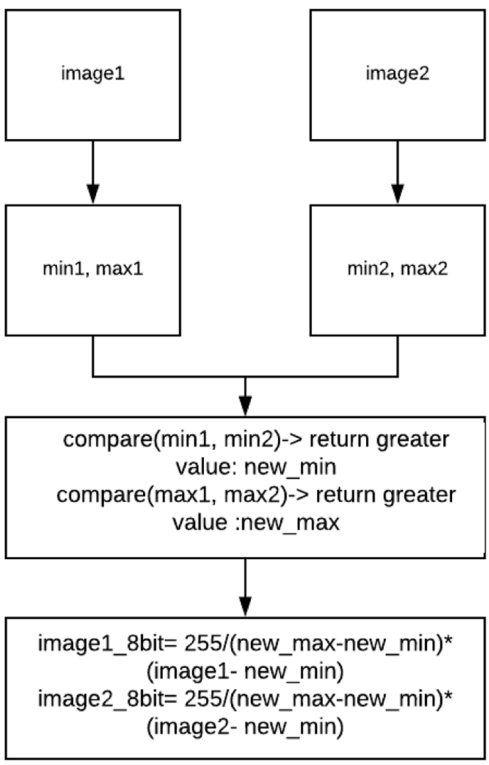

FIGURE 5 Our proposed scaling algorithm from two raw fourteen bit images. Minimum and maximum pixel values are extracted from each frame, with the logic returning greatest range. Two new eight bit frames with the same scale can be reconstructed from the new maximum and minimum values

Figure 7 illustrates before and after the scaling factor produced using the proposed technique is applied on two consecutive frames captured at 1400 h Australian Central Daylight Time (ACDT) on the test day.

Table 1 shows the comparison of pixel intensities of a pair of images from Figures 4 and 7. It is clear that optical flow cannot be computed from images in Figure 4 due to brightness inconstancy. While in Figure 7, the brightness across them is consistent, satisfying the first assumption for computing optical flow.

5.2.3 | Optical flow pyramid LK settings in OpenCV

Optical flow estimation was based on the OpenCV Pyramid LK implementation. The algorithm takes two eight bit, 160x120 resolution images, scaled described, as input. Reliable features were found based on the Shi-Tomasi corner detection algorithm (Shi, 1994). The output of the algorithm is single displacement vectors in two dimensions as a median of all good points found (Table 2).

6 | ASSESSMENT METHODOLOGY

In this section, we present the drone that was used in this study. Details of the experimental site, flight plan and the methodology that we used to assess the performance of the thermal flow sensor are presented.

6.1 | Flying platform

A 3DR Robotics SOLO quadrotor (SOLO) was used for this experiment. The SOLO can take off with a payload attached of up to 500 g, during mild to strong wind conditions. With a 5200 mAh lithium polymer battery, flight endurance is up to 10 min with the payload attached. Figure 8 shows the SOLO at the experimental site.

6.2 | Experimental site

The flight test was conducted over agricultural land in South Australia. The site has been selected due to its suitability for gaining approval for day/night operations and its flat ground. The test site provides a clear sky view, far from urban areas, contains limited artificial objects and no obstacles on the ground such as large tress or rocks.

The experiment was done in late summer in a 24 h period during which the weather varied. The weather was warm on the afternoon of the first day: 29°C at noon and as low as 13°C in the early morning (Bureau of Meteorology, 2020). In the first 16 h, wind was mild at 15 km/h. Late in the experimental period, a front brought strong wind at approximately 40 km/h with a temperature at noon of 27°C. Table 3 shows sunrise, sunset, max, and min temperature for the site.

Figure 9 shows the Lux meter reading for each run. There are zero lux reading between 2200 h and 0600 h, during which

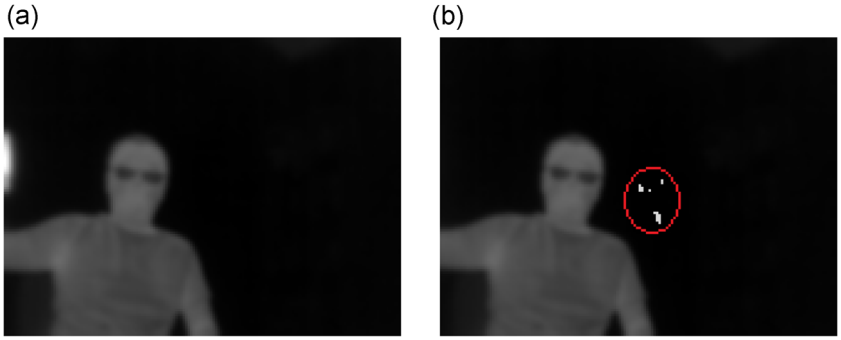

FIGURE 6 Change of contrast with our proposed techniques. There are a few small artifacts in the images- color in red circle, the impact is minimal. (a) Frame 1 and (b) Frame 2

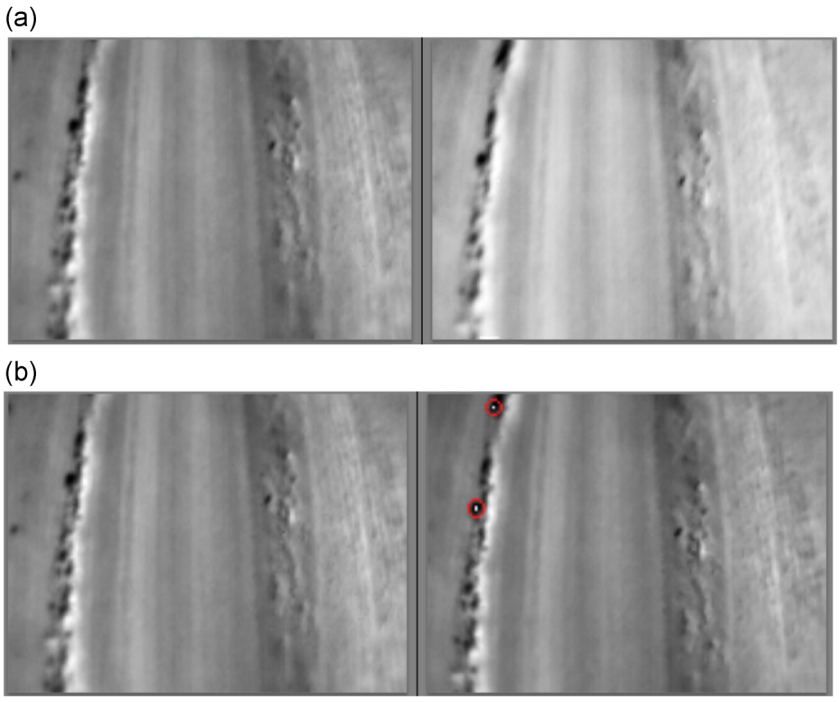

FIGURE 7 Comparison of AGC and our technique with one pair of frames captured at the site. Small artifacts are highlighted with red circles. (a) A pair of thermal frames captured at the site processed with the AGC and (b) a pair of thermal frames captured at the site processed with the proposed technique. AGC, automatic gain control

TABLE 1 Pixel intensity value comparison

	Mean	90% percentile	10% percentile
Processed with AGC			
Img1	122	155	95
Img2	154	205	145
Processed with the proposed technique			
Img1	122	155	95
Img2	123	156	96

TABLE 2 Parameter settings for the LK Optical flow and Shi-Tomasi corner detection algorithm

Feature Detection Setting	Maximum corners	1000
	Quality level	0.02
	Minimum distance	5
	Block size	5
LK Settings	Window size	(15,15)
	Maximum pyramid level	2
	Search termination count	10
	Search termination ε	0.03

time we did not expect the PX4Flow to function. There was low lux at 2000 h, indicating likely low performance of the PX4Flow.

6.3 | Flight plan

The SOLO carrying the sensor was programmed to fly one square lap at a constant height of 10 m using GPS waypoint navigation, with a target velocity of 10 m/s. The SOLO was pointing in the same direction throughout the experiment. Figure 10 shows the flight plan in Mission Planner software. The SOLO took off at point (1) then followed the main road to begin the mission following a square path. With these settings of height above ground and speed, the translational motion of the drone causes an effective per-frame angular change of the

FIGURE 8 Drone at the site waiting to take off at noon. The drone faced north during the entire flight

TABLE 3 Experimental site temperature and wind conditions at the time of the experiment

Sunrise	06:58
Sunset	19:59
Max temperature	29°C
Min temperature	13°C

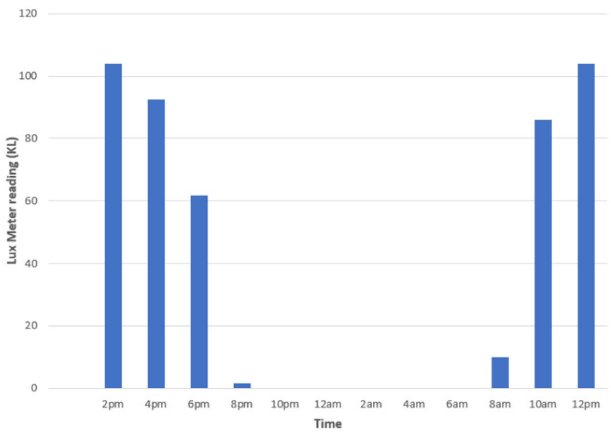

FIGURE 9 Lux meter readings over 24 h

image across the image plane of approximately 7°. The FOV of the lepton is 50° which is sufficiently large that the apparent motion can be considered small, meeting the assumptions of optical flow and suggesting that the configuration is suited to further evaluation.

From point (1)-(2), the drone follows a dirt road without any vegetation. At point (2), there is substantial texture on the ground. From point (2)-(3)-(4)-(5), the drone flew over a mostly empty wheat field in stubble. We selected three locations on the site with distinctive features to examine their thermal data over 24h, as shown in Figure 11.

FIGURE 10 Mission Plan shown in the Mission Planner software. The drone took off at point (1), then follow point (2)-(3)-(4) then landed at point (5)

6.4 | 24-h flight test

Thermal flow relies on reflected and radiated heat from the environment. There are many different objects on the ground such as grass, rocks, branches, etc. Each type of object has different thermal mass and the ability to absorb and release heat at different rates (Yang & Li, 2008). Hence, the heat map will vary greatly across a day. Therefore, our plan was to perform the experiments at different times to investigate how features varied during day and night and how thermal flow is affected by these changes.

A flight test was conducted at the site every 2 h over a 24 h period, for a total of 12 flights. For each flight, data logs were recorded, including thermal flow, optical flow, range finder and GPS location. From the data logs, thermal and optical flow plots were used to evaluate their performance for each flight.

7 | EXPERIMENTAL RESULTS

In this section, we present the flight test results to compare optical flow (OF) and thermal flow (TF) performance. Our analysis includes: distinct features present in thermal frames based on magnitude spectrum, standard deviation value of pixel intensity of images and signals matching based on normalized cross correlation.

7.1 | Features during 24 h

In this section, the three distinctive parts of the test site are presented in Figure 11: at the top left corner, the wheat field and the main road. The inverse fast Fourier transform was applied to each image to obtain the magnitude spectrum, to explore how spatial frequencies vary during 24 h. For TF to work well, there should be a balance of low and high spatial frequencies in the frame, which

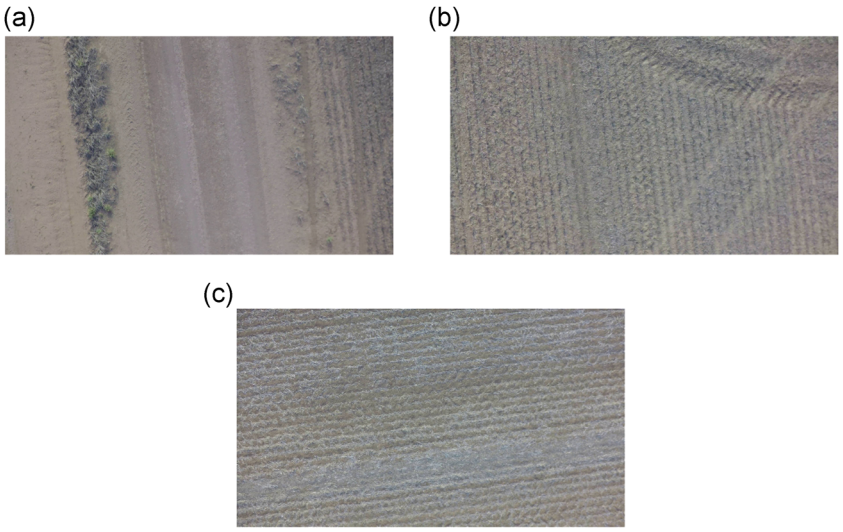

FIGURE 11 RGB images of the site showing three different interesting features of the site, which were examined throughout 24 h. (a) RGB image over the dirt road (1)-(2), (b) RGB image at point (2), and (c) RGB image over the wheat field (2)-(5)

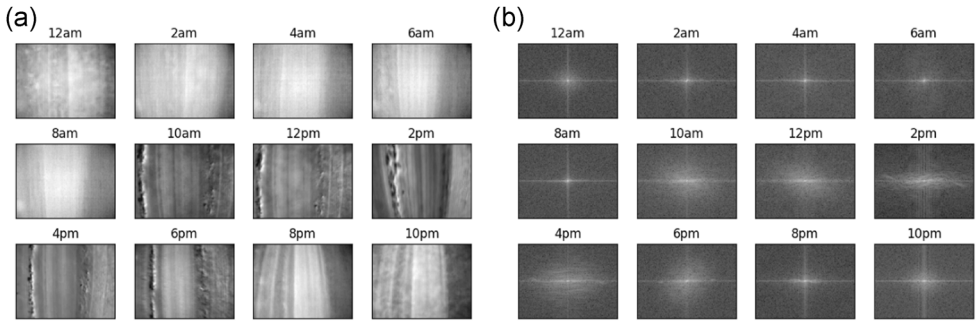

FIGURE 12 Thermal frames and magnitude spectrum of the main road over 24 h. (a) Thermal frames of the main road and (b) magnitude spectrum of the main road

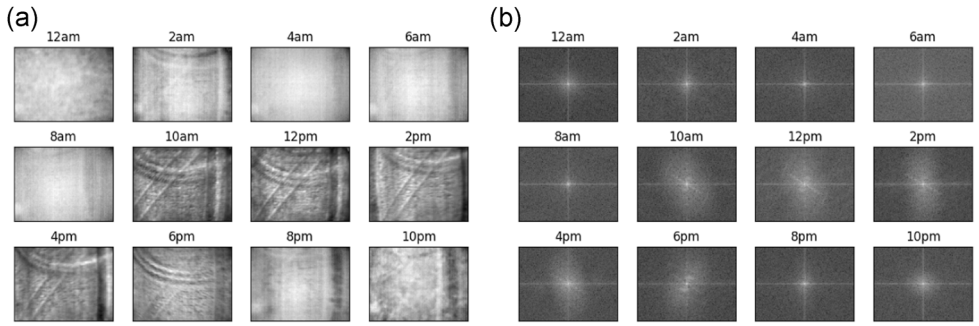

FIGURE 13 Thermal frames and magnitude spectrum of the top corner over 24 h. (a) Thermal frames of the top corner and (b) magnitude spectrum of the top corner

means there are more distinct features for the Shi-Tomasi algorithm to detect for the LK.

Figures 12–14 show thermal frames and their respective magnitude spectrum over 24 h.

Generally, the best features were found from 1000 h to 2000 h across the three locations. During the night and early morning from 2200 h to 0800 h, there were fewer features visible on the ground. Interestingly, features became apparent again at 0200 h at the wheat field. This can be explained as parts of the ground, the air and the wheat stubble have different thermal conductivity and thermal capacity (Ho et al., 1972). Additionally, this suggests that high spatial frequency features became fewer with time after sunset since all of the small surface features soak to the same temperature, and the primary features remaining were then large structures in the ground.

Table 4 shows numbers of detected features to track from above thermal frames, with parameters as in Table 2. The results show that there were substantially more features that could be detected between 0600 h and 1800 h. For the period between 2000 h and

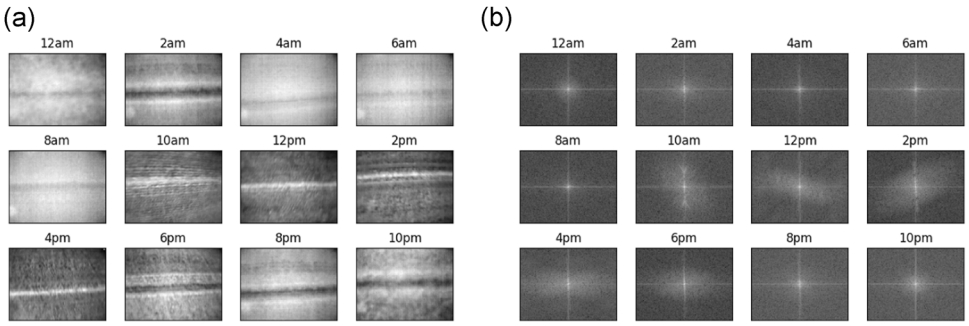

FIGURE 14 Thermal frames and magnitude spectrum over 24 h. (a) Thermal frames of the wheat field and (b) magnitude spectrum of the wheat field

TABLE 4 Features found with Shi-Tomasi algorithm over three locations of the site over 24 h

	Main road	Wheat field	Top corner
0000 h	2	2	1
0200 h	3	12	8
0400 h	2	1	0
0600 h	11	6	4
0800 h	8	6	5
1000 h	15	14	25
1200 h	21	19	29
1400 h	25	21	31
1600 h	27	22	32
1800 h	22	17	21
2000 h	12	8	3
2200 h	8	7	4

Note: There are substantially more detected features in all locations during late morning until just after dark. 0200 h was an exception with more detected features.

TABLE 5 Standard deviation of pixel intensity at three locations over 24 h

	Main road	Wheat field	Top corner
0000 h	36.07	35.03	33.41
0200 h	33.7	34.53	36.36
0400 h	38.03	29.4	39.2
0600 h	43.1	29.4	29.54
0800 h	40.56	27.37	29.11
1000 h	26.34	31.43	31.93
1200 h	26.15	35.41	34.37
1400 h	31.8	32.7	36.67
1600 h	22.9	32.14	31.1
1800 h	33.57	36.7	31.96
2000 h	45.5	34.25	36.43
2200 h	49.8	37.67	36.9

0400 h, the number of detected features diminished substantially, except there was a small increase at 0200 h. These results are consistent with the magnitude spectrum data.

Table 5 shows standard deviation value of pixel intensity for images as shown in Figures 12–14, to measure the amount of power away from the mean value. The data suggests that features varied quite a lot at the main road compared to the wheat field and top corner. It shows that the TF performance is substantially effected in the open field area during heating and cooling cycles.

7.2 | Signals

In this section, the overlay of OF and TF flow signals will be presented, including X displacement, Y displacement and the normalized cross correlation for both TF and OF. We present the five most significant results from our trial which were early afternoon at 1400 h, after dark at 2000 h, midnight at 0000 h, at 1400 h and after sunrise at 0800 h. The rest of the data is presented in Appendix A including Figures A1–A7.

The PX4Flow reports data to the autopilot at 10Hz while the Lepton operates at 8.7 Hz, there will be errors caused by misalignment of the sampling instants of the two signals (Rosser et al., 2021). In the end, the numerical analysis data will be presented in one table.

7.2.1 | 1400 h

Figure 16 shows OF and TF signal at 1400 h. The strong correlation value shows TF works well compared to OF. Strong correlation means the signals were well matched. Notably the OF signal at +Y displacement was quite weak compared to TF, indicating that OF did not work well on the main road. The main road may have caused a correspondence problem, caused by lack of information on one axis, "the aperture problem" Xue et al. (2015) with the block matching algorithm while the LK did not suffer from this problem. Furthermore, the PX4Flow captures images in a 4 × 4 binned cropped image that can also cause the aperture problem to appear as illustrated in Figure 15 (Figure 16).

7.2.2 | 2000 h

Figure 17 shows OF and TF signals at 2000 h just after the sunset. TF also shows a good signal compared to OF, and the aperture problem becomes more apparent as the night progresses.

7.2.3 | 0000 h

Figure 18 shows, unsurprisingly, OF does not work at night while TF works at some degree during this time. A low correlation value confirms this.

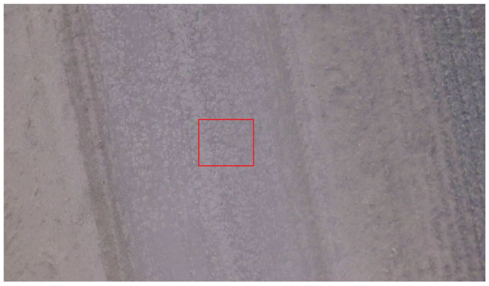

FIGURE 15 PX4Flow cropped mode as highlighted in red

7.2.4 | 0200 h

Interestingly, more distinct features were observed at 0200 h compared to other samples taken at night as shown on Figure 19. TF works better at 0200 h than previous 0000 h, especially over the wheat field.

7.2.5 | 0800 h

Figure 20 shows that OF works well after sunrise when the ground is properly illuminated. On the other hand, TF works well with Y displacement but not so well with X displacement. This means because the main road heats up faster than the wheat field, there are more features to be found on the main road for the LK algorithm to track.

Table 6 shows the maximum correlation values in X and Y displacement for 24 h.

8 | DISCUSSION

The thermal flow results show that optical flow can be estimated from compact, low resolution and affordable thermal image planes for aerial applications. We have shown that thermal flow works comparably well to PX4Flow during early morning to just after

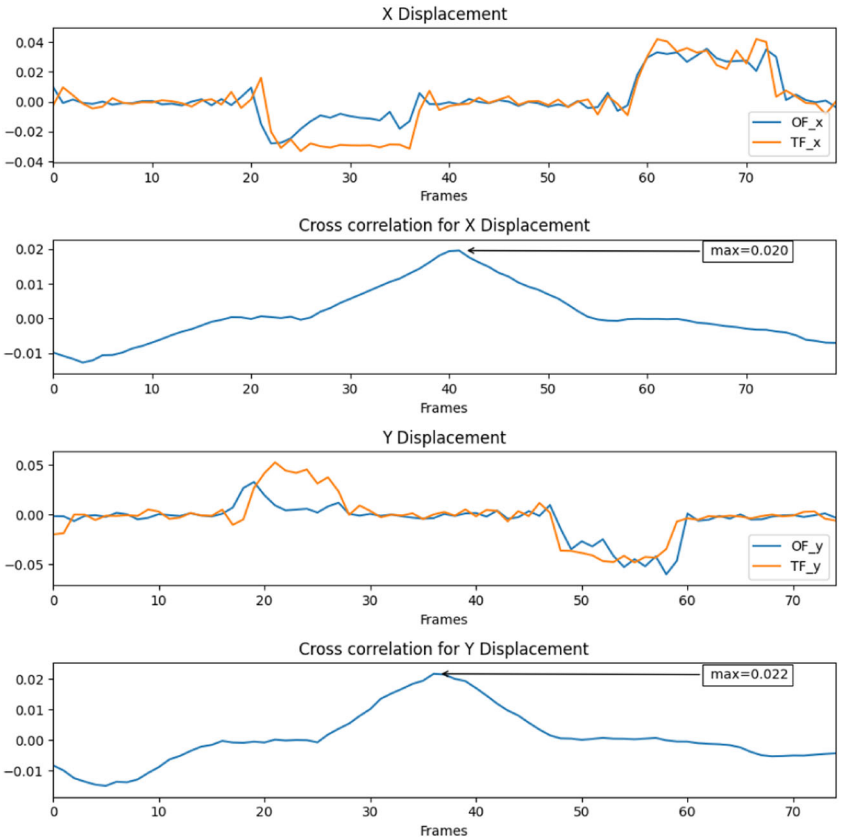

FIGURE 16 OF and TF signals at 1400 h. OF, optical flow; TF, thermal flow

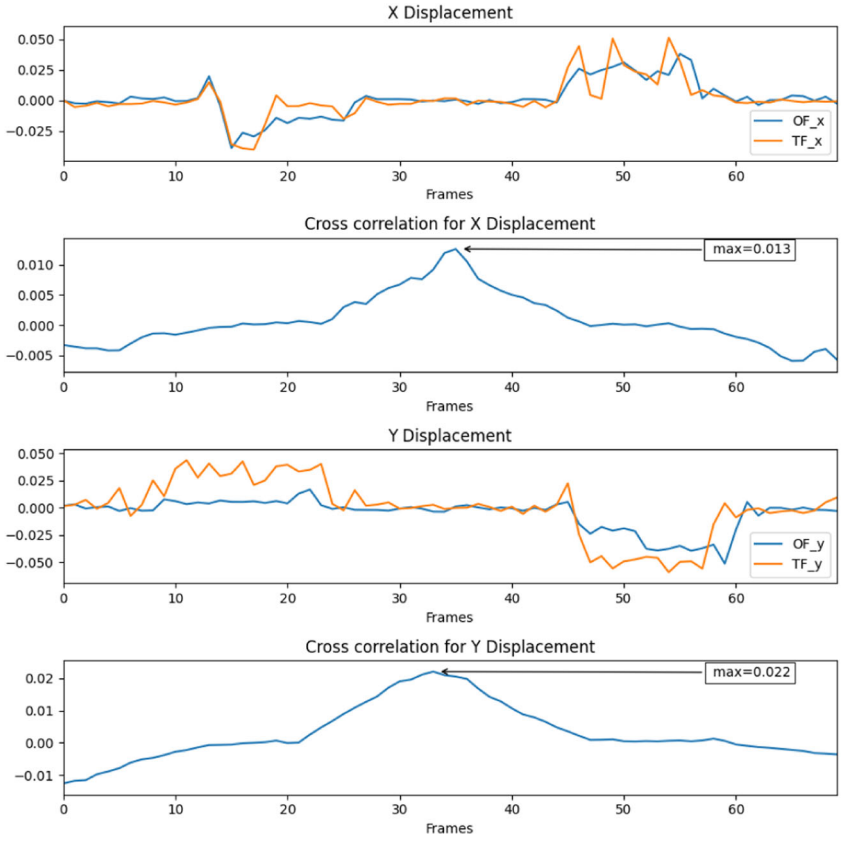

FIGURE 17 OF and TF signals at 2000 h. OF, optical flow; TF, thermal flow

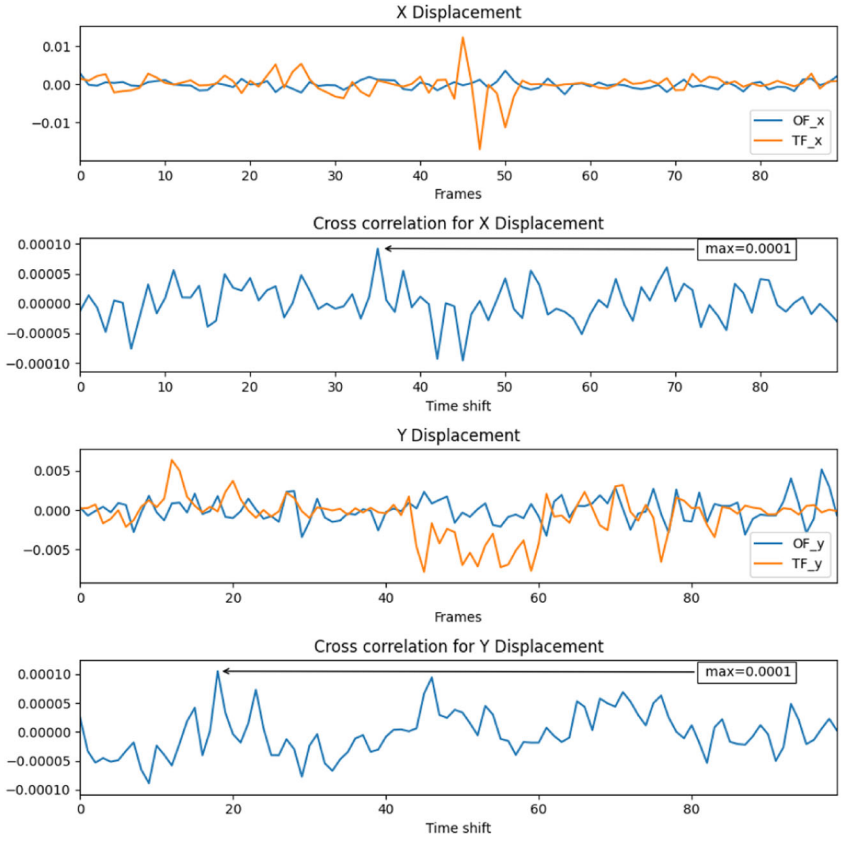

FIGURE 18 OF and TF signals at 0000 h. OF, optical flow; TF, thermal flow

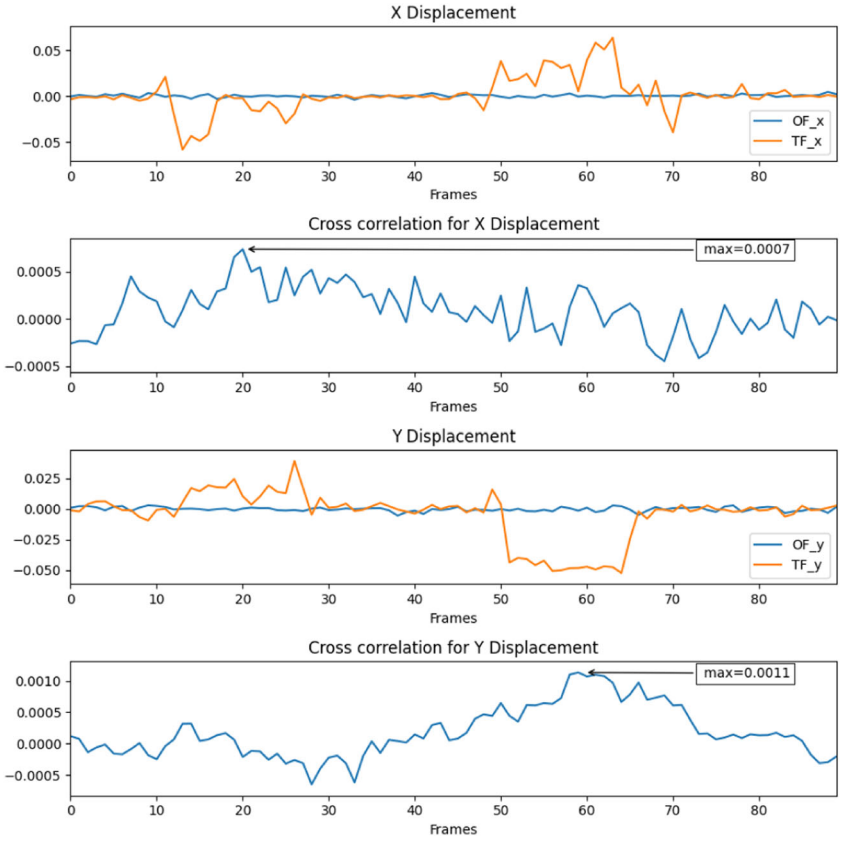

FIGURE 19 OF and TF signals at 0200 h. OF, optical flow; TF, thermal flow

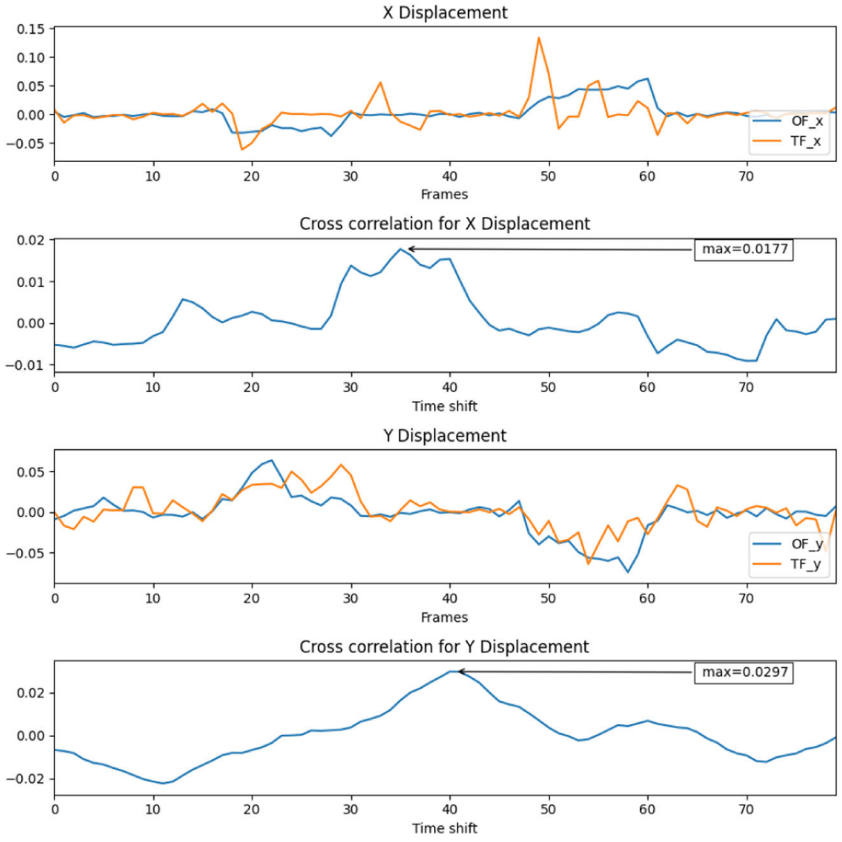

FIGURE 20 OF and TF signals at 0800 h. OF, optical flow; TF, thermal flow

TABLE 6 Maximum cross correlation value of X and Y displacements over 24 h

Time	Max cross correlation of X displacement	Max cross correlation of Y displacement
0000 h	0.0001	0.0001
0200 h	0.0007	0.0011
0400 h	0.0007	0.0006
0600 h	**0.0275**	**0.036**
0800 h	**0.017**	**0.029**
1000 h	**0.021**	**0.025**
1200 h	**0.03**	**0.027**
1400 h	**0.02**	**0.022**
1600 h	**0.029**	**0.026**
1800 h	**0.048**	**0.054**
2000 h	0.0002	0.0001
2200 h	0.0002	0.0001

Note: The bold values indicate higher cross correlation values in X and Y displacements, which translate to better performance of thermal flow at those time.

sunset. Furthermore, thermal flow continues to function with lower accuracy during night when conventional optical sensors see nothing.

From the output signal plots during the night, Figures 18 and 19, optical flow did not function, while thermal flow worked to some degree. From Figure 20, optical flow performed well, while thermal flow performed poorly in the X displacement, at the main road. This can be explained as during early morning, the environments needs some time to heat up which can lead to less features for thermal flow. At other times, thermal flow worked similarly to optical flow.

The LK algorithm relies on contrast and distinct features in the first frame, with Shi-Tomasi Shi (1994) finding good features to track. For thermal frames, these features rely on the difference in temperature between objects and the surrounding environment. After sunset, heat is slowly released and all things on the surface and under the surface cool. This makes thermal flow of variable quality after dark, but on this night it worked to some degree using available warm features on and under the ground.

9 | CONCLUSION

In conclusion, we have shown that determining optical flow from low resolution thermal imagery for real-time aerial applications is possible. Furthermore, thermal flow performance over a full hot and cold cycle was analyzed. Thermal flow works well after early morning until midnight. During other times of night and early morning, thermal flow functioned to some degree but is less reliable. Furthermore, the TF does not suffer from aperture problem from as shown on the main road in this study.

This study shows that relying on distinct features from thermal frames for optical flow estimation was unreliable, especially after sunset. It is clear that an algorithm must be identified that is less reliant on corner features, while also being fast.

Second, by down sampling fourteen bit images to eight bit for compatibility with the highly optimized existing implementation in OpenCV and to ensure real-time performance, lots of information was discarded (Bloesch et al., 2017). Therefore, there is a need to develop a variation of this algorithm that can utilize full fourteen bit raw images directly from the lepton. Using fourteen bit images, there is no need to recalculate the scale for each pair of images and the heat map can be used directly.

The research has been conducted on one site only, future research will look at different sites with different environmental structures and conditions.

Subsequent research is intended to implement a high bit depth algorithm probably using 32 bits to allow for future sensors. Additionally, future work will focus on algorithms and behaviors for navigation and control that are well suited to low resolution and low thermal contrast conditions.

ACKNOWLEDGMENTS

This study was supported by an Australian Government Research Training Program (RTP) Scholarship. The authors would like to thank the Aerospace Division of the Defence Science and Technology Group (DST Group) for conducting the night part of the trial and the Royal Australian Air Force for authorizing the night flights. Open access publishing facilitated by University of South Australia, as part of the Wiley - University of South Australia agreement via the Council of Australian University Librarians.

ORCID

Tran Xuan Bach Nguyen https://orcid.org/0000-0002-9914-2265
Kent Rosser https://orcid.org/0000-0003-4017-6396

REFERENCES

Al-Naji, A., Gibson, K., Lee, S.-H. & Chahl, J. (2017) Monitoring of cardiorespiratory signal: principles of remote measurements and review of methods. *IEEE Access*, *5*, 15776–15790.

Al-Naji, A., Perera, A.G. & Chahl, J. (2017) Remote monitoring of cardiorespiratory signals from a hovering unmanned aerial vehicle. *Biomedical Engineering Online*, *16*(1), 101.

Al-Naji, A., Perera, A.G. & Chahl, J. (2018) Remote measurement of cardiopulmonary signal using an unmanned aerial vehicle. In: *IOP Conference Series: Materials Science and Engineering* (Vol. 405), AEROTECH VII - Sustainability in Aerospace Engineering and Technology 7–8 August 2018. Putrajaya, Malaysia: IOP Publishing, p. 012001.

Alchanatis, V., Cohen, Y., Cohen, S., Moller, M., Sprinstin, M., Meron, M. et al. (2010) Evaluation of different approaches for estimating and mapping crop water status in cotton with thermal imaging. *Precision Agriculture*, *11*(1), 27–41.

Baker, S., Scharstein, D., Lewis, J., Roth, S., Black, M.J. & Szeliski, R. (2011) A database and evaluation methodology for optical flow. *International Journal of Computer Vision*, *92*(1), 1–31.

Barrows, G.L., Chahl, J.S. & Srinivasan, M.V. (2002) Biomimetic visual sensing and flight control. In: *Proc. Bristol UAV Conf*. Citeseer, pp. 1–15.

Beauchemin, S.S. & Barron, J.L. (1995) The computation of optical flow. *ACM Computing Surveys (CSUR)*, *27*(3), 433–466.

Bloesch, M., Burri, M., Omari, S., Hutter, M. & Siegwart, R. (2017) Iterated extended Kalman filter based visual-inertial odometry using direct photometric feedback. *The International Journal of Robotics Research*, *36*(10), 1053–1072.

Borges, P.V.K. & Vidas, S. (2016) Practical infrared visual odometry. *IEEE Transactions on Intelligent Transportation Systems*, *17*(8), 2205–2213.

Bouguet, J.-Y. (2001) Pyramidal implementation of the affine Lucas Kanade feature tracker description of the algorithm. Intel Corporation, 5(1–10), 4.

Bradski, G. (2000) The OpenCV library. Dr. Dobb's Journal: Software Tools for the Professional Programme, *25*(11), 120–123.

Brunner, C., Peynot, T., Vidal-Calleja, T. & Underwood, J. (2013) Selective combination of visual and thermal imaging for resilient localization in adverse conditions: Day and night, smoke and fire. *Journal of Field Robotics*, *30*(4), 641–666.

Bureau of Meteorology. (2020). *Mallala weather*.

Camus, T. (1995) *Calculating time-to-contact using real-time quantized optical flow* (*14*). Tübingen, Germany: Max Planck Institute for Biological Cybernetics.

Chahl, J. & Mizutani, A. (2006) An algorithm for terrain avoidance using optical flow. In: *2006 American Control Conference 14-16 June 2006*. Minneapolis, Minnesota USA: IEEE, p. 6.

Chahl, J., Mizutani, A., Strens, M. & Wehling, M. (2005) Autonomous navigation using passive sensors and small computers. In: *Infotech@ Aerospace*, 83, p. 7013.

Chahl, J.S., Srinivasan, M.V. & Zhang, S.-W. (2004) Landing strategies in honeybees and applications to uninhabited airborne vehicles. *The International Journal of Robotics Research*, *23*(2), 101–110.

Cruz, G. & Bernardino, A. (2016) Aerial detection in maritime scenarios using convolutional neural networks. In: *International Conference on Advanced Concepts for Intelligent Vision Systems 24-27 October*. Lecce, Italy: Springer, pp. 373–384.

Dabov, K., Foi, A., Katkovnik, V. & Egiazarian, K. (2006) Image denoising with block-matching and 3d filtering. In: *Image Processing: Algorithms and Systems, Neural Networks, and Machine Learning* (Vol. 6064). International Society for Optics and Photonics, p. 606414.

Delaune, J., Hewitt, R., Lytle, L., Sorice, C., Thakker, R. & Matthies, L. (2019) Thermal-inertial odometry for autonomous flight throughout the night. In: *2019 IEEE/RSJ International Conference on Intelligent Robots and Systems (IROS)*. Macau: IEEE, pp. 1122–1128.

Dusha, D., Boles, W. & Walker, R. (2007) Attitude estimation for a fixed-wing aircraft using horizon detection and optical flow. In: *9th Biennial Conference of the Australian Pattern Recognition Society on Digital Image Computing Techniques and Applications (DICTA 2007) 3-5 Dec. 2007*. Glenelg, SA, Australia: IEEE, pp. 485–492.

Esch, H. & Burns, J. (1996) Distance estimation by foraging honeybees. *Journal of Experimental Biology*, *199*(1), 155–162.

Farnebäck, G. (2003) Two-frame motion estimation based on polynomial expansion. In *Scandinavian Conference on Image analysis* (pp. 363–370). Halmstad, Sweden: Springer.

Fernandes, R.A. (1989) *Monitoring system for power lines and right-of-way using remotely piloted drone*. US Patent 4,818,990.

FLIR Corp. (2018) *FLIR Lepton engineering data sheet*. Wilsonville, Oregon, U.S.: FLIR Corp.

Franz, M.O., Chahl, J.S. & Krapp, H.G. (2004) Insect-inspired estimation of egomotion. *Neural Computation*, *16*(11), 2245–2260.

Gan, S.K. & Sukkarieh, S. (2011) Multi-UAV target search using explicit decentralized gradient-based negotiation. In: *2011 IEEE International Conference on Robotics and Automation 9-13 May 2011*. Shanghai, China: IEEE, pp. 751–756.

Garmin. (2016) *Lidar Lite v3 Operation Manual and Technical Specifications*. Olathe, Kansas, U.S.: Garmin.

Garratt, M. & Chahl, J. (2003) Visual control of an autonomous helicopter. In: *41st Aerospace Sciences Meeting and Exhibit*, p. 460.

Gonzalez-Dugo, V., Zarco-Tejada, P., Nicolás, E., Nortes, P.A., Alarcón, J. et al. (2013) Using high resolution uav thermal imagery to assess the variability in the water status of five fruit tree species within a commercial orchard. *Precision Agriculture*, *14*(6), 660–678.

Ho, C.Y., Powell, R.W. & Liley, P.E. (1972) Thermal conductivity of the elements. *Journal of Physical and Chemical Reference Data*, *1*(2), 279–421.

Honegger, D., Meier, L., Tanskanen, P. & Pollefeys, M. (2013). An open source and open hardware embedded metric optical flow CMOS camera for indoor and outdoor applications. In: *2013 IEEE International Conference on Robotics and Automation 6-10 May*. Karlsruhe, Germany: IEEE, pp. 1736–1741.

Horn, B.K. & Schunck, B.G. (1981) Determining optical flow. In: *Techniques and Applications of Image Understanding* (Vol. 281). International Society for Optics and Photonics, pp. 319–331.

Jordan, S., Moore, J., Hovet, S., Box, J., Perry, J., Kirsche, K., et al. (2017) State-of-the-art technologies for UAV inspections. *IET Radar, Sonar & Navigation*, *12*(2), 151–164.

Khattak, S., Papachristos, C. & Alexis, K. (2018) Marker based thermal-inertial localization for aerial robots in obscurant filled environments. In: *International Symposium on Visual Computing*. Springer, pp. 565–575.

Khattak, S., Papachristos, C. & Alexis, K. (2019) Visual-thermal landmarks and inertial fusion for navigation in degraded visual environments. In: *2019 IEEE Aerospace Conference* March 2019. Big Sky, Montana, USA: IEEE, pp. 1–9.

Khattak, S., Papachristos, C. & Alexis, K. (2020) Keyframe-based thermal-inertial odometry. *Journal of Field Robotics*, *37*(4), 552–579.

Lu, Y., Xue, Z., Xia, G.-S. & Zhang, L. (2018) A survey on vision-based UAV navigation. *Geo-Spatial Information Science*, *21*(1), 21–32.

Lucas, B.D. & Kanade, T. (1981) An iterative image registration technique with an application to stereo vision. Vancouver, BC.

Meron, M., Sprintsin, M., Tsipris, J., Alchanatis, V. & Cohen, Y. (2013) Foliage temperature extraction from thermal imagery for crop water stress determination. *Precision Agriculture*, *14*(5), 467–477.

Miller, A., Miller, B., Popov, A. & Stepanyan, K. (2018) Optical flow as a navigation means for UAV. In: *2018 Australian & New Zealand Control Conference (ANZCC)*. Melbourne, Australia: IEEE, pp. 302–307.

Mouats, T., Aouf, N., Chermak, L. & Richardson, M.A. (2015) Thermal stereo odometry for UAVs. *IEEE Sensors Journal*, *15*(11), 6335–6347.

Mouats, T., Aouf, N., Nam, D. & Vidas, S. (2018) Performance evaluation of feature detectors and descriptors beyond the visible. *Journal of Intelligent & Robotic Systems*, *92*(1), 33–63.

Papachristos, C., Mascarich, F. & Alexis, K. (2018) Thermal-inertial localization for autonomous navigation of aerial robots through obscurants. In: *2018 International Conference on Unmanned Aircraft Systems (ICUAS) 12-15 June 2018*. Dallas, U.S.: IEEE, pp. 394–399.

Perera, A.G., Law, Y.W. & Chahl, J. (2018) Human pose and path estimation from aerial video using dynamic classifier selection. *Cognitive Computation*, *10*(6), 1019–1041.

Perera, A.G., Law, Y.W. & Chahl, J. (2019) Drone-action: an outdoor recorded drone video dataset for action recognition. *Drones*, *3*(4), 82.

Rosser, K. & Chahl, J. (2019) Reducing the complexity of visual navigation: Optical track controller for long-range unmanned aerial vehicles. *Journal of Field Robotics*, *36*(6), 1118–1140.

Rosser, K., Nguyen, T.X.B., Moss, P. & Chahl, J. (2021) Low complexity visual UAV track navigation using long-wavelength infrared. *Journal of Field Robotics*, *38*(6), 882–897.

Sato, S. & Anezaki, T. (2017) Autonomous flight drone for infrastructure (transmission line) inspection (2). In: *2017 International Conference on Intelligent Informatics and Biomedical Sciences (ICIIBMS) Nov 2017*. Okinawa, Japan: IEEE, pp. 294–296.

Shi, J. & Tomasi, C. (1994) Good features to track. In: *1994 Proceedings of IEEE Conference on Computer Vision and Pattern Recognition*. Seattle, WA, USA: IEEE, pp. 593–600.

Srinivasan, M.V. (1994) An image-interpolation technique for the computation of optic flow and egomotion. *Biological Cybernetics*, *71*(5), 401–415.

Srinivasan, M.V. (2010) Honey bees as a model for vision, perception, and cognition. *Annual Review of Entomology*, *55*1, 267–284.

Srinivasan, M.V., Chahl, J.S., Weber, K., Venkatesh, S., Nagle, M.G. & Zhang, S.-W. (1999) Robot navigation inspired by principles of insect vision. *Robotics and Autonomous Systems*, *26*(2–3), 203–216.

Srinivasan, M.V., Zhang, S., Altwein, M. & Tautz, J. (2000) Honeybee navigation: nature and calibration of the "odometer". *Science*, *287*(5454), 851–853.

Srinivasan, M.V., Zhang, S.-W., Chahl, J.S., Barth, E. & Venkatesh, S. (2000) How honeybees make grazing landings on flat surfaces. *Biological Cybernetics*, *83*(3), 171–183.

Varghese, A., Gubbi, J., Sharma, H. & Balamuralidhar, P. (2017) Power infrastructure monitoring and damage detection using drone captured images. In: *2017 International Joint Conference on Neural Networks (IJCNN)*. Anchorage, Alaska, USA: IEEE, pp. 1681–1687.

Xue, T., Mobahi, H., Durand, F. & Freeman, W.T. (2015) The aperture problem for refractive motion. In: *Proceedings of the IEEE Conference on Computer Vision and Pattern Recognition 7-12 June*. Boston, MA, USA: IEEE, pp. 3386–3394.

Yang, L. & Li, Y. (2008) Cooling load reduction by using thermal mass and night ventilation. *Energy and Buildings*, *40*(11), 2052–2058.

Zingg, S., Scaramuzza, D., Weiss, S. & Siegwart, R. (2010) MAV navigation through indoor corridors using optical flow. In: *2010 IEEE International Conference on Robotics and Automation 3-8 May*. Anchorage, Alaska: IEEE, pp. 3361–3368.

Zufferey, J.-C. & Floreano, D. (2005) Toward 30-gram autonomous indoor aircraft: vision-based obstacle avoidance and altitude control. In: *Proceedings of the 2005 IEEE International Conference on Robotics and Automation 18-22 April*. Barcelona, Spain: IEEE, pp. 2594–2599.

SUPPORTING INFORMATION

Additional supporting information may be found in the online version of the article at the publisher's website.

How to cite this article: Nguyen, T.X.B., Rosser, K., Perera, A., Moss, P., Teague, S. & Chahl, J. (2022) Characteristics of optical flow from aerial thermal imaging, "thermal flow". *Journal of Field Robotics*, 39, 580–599. https://doi.org/10.1002/rob.22065

APPENDIX A

See Figure A1–A7

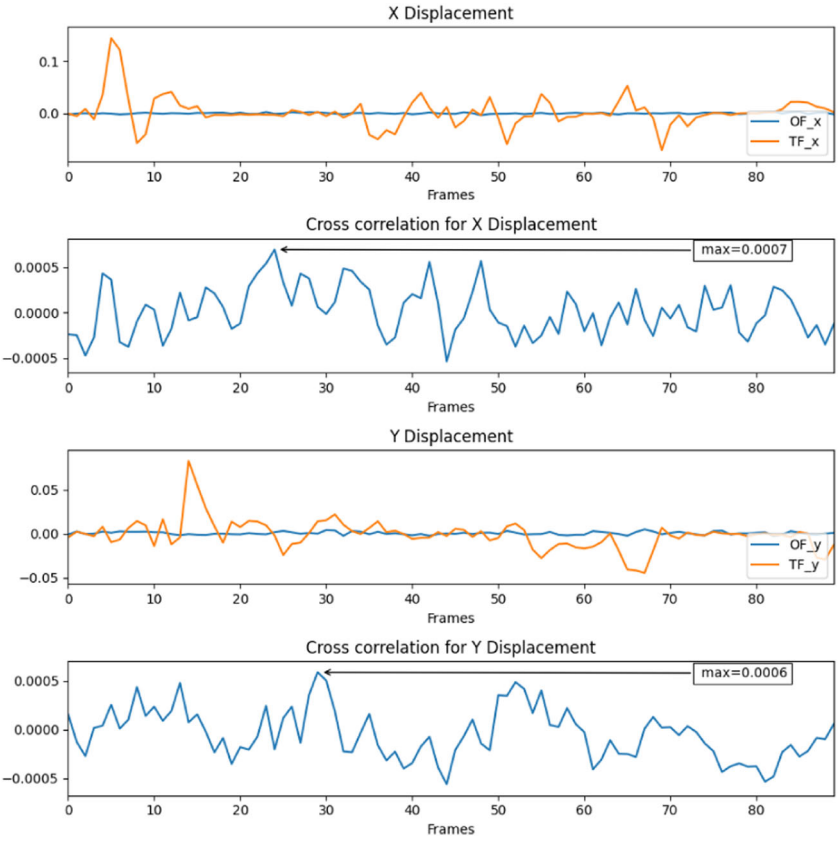

FIGURE A1 OF and TF signals at 0400 h. OF, optical flow; TF, thermal flow

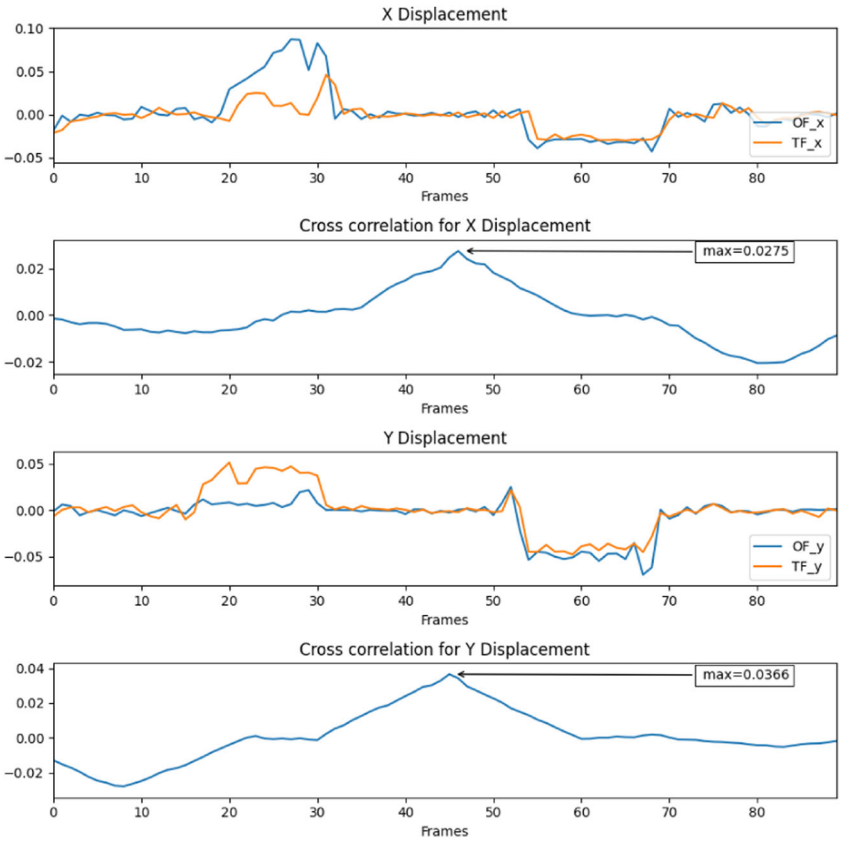

FIGURE A2 OF and TF signals at 0600 h. OF, optical flow; TF, thermal flow

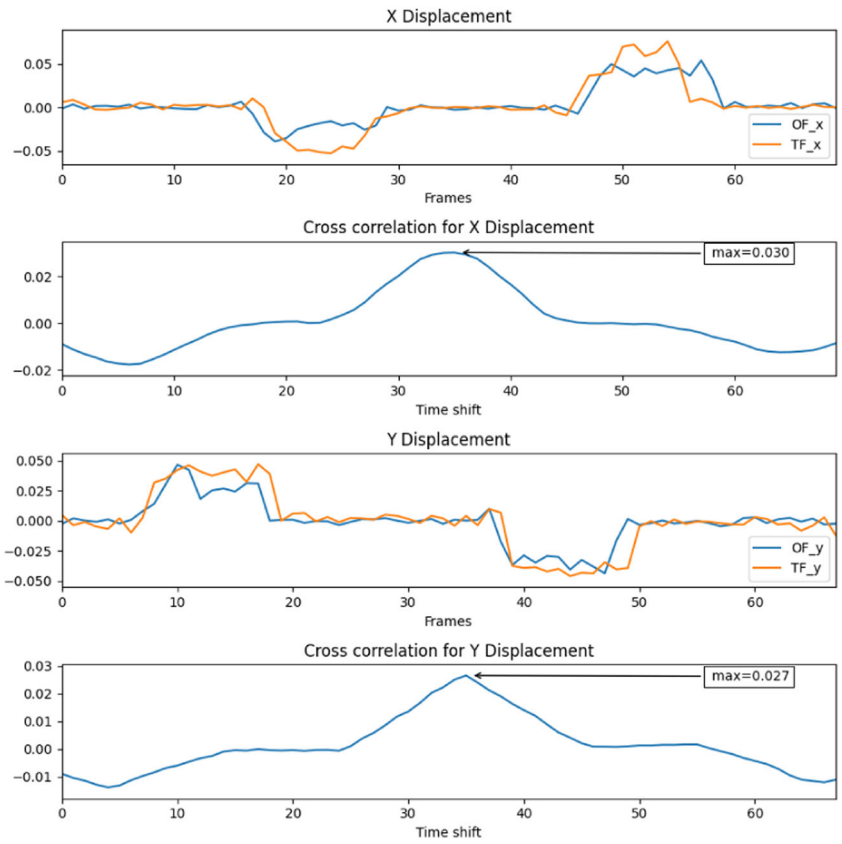

FIGURE A3 OF and TF signals at 1000 h. OF, optical flow; TF, thermal flow

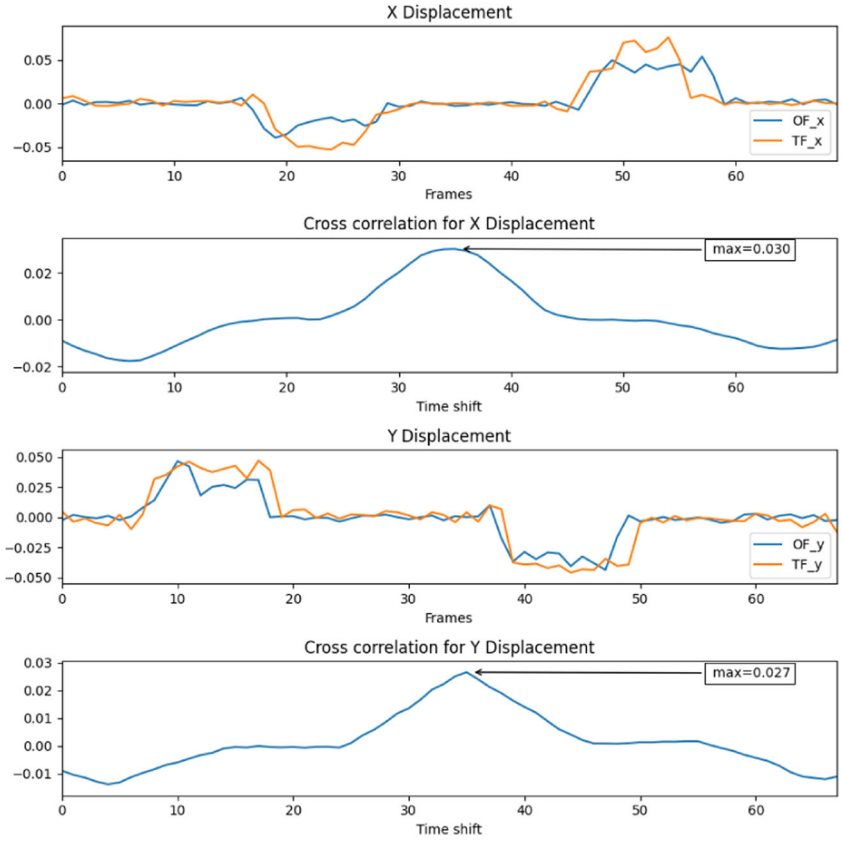

FIGURE A4 OF and TF signals at 1200 h. OF, optical flow; TF, thermal flow

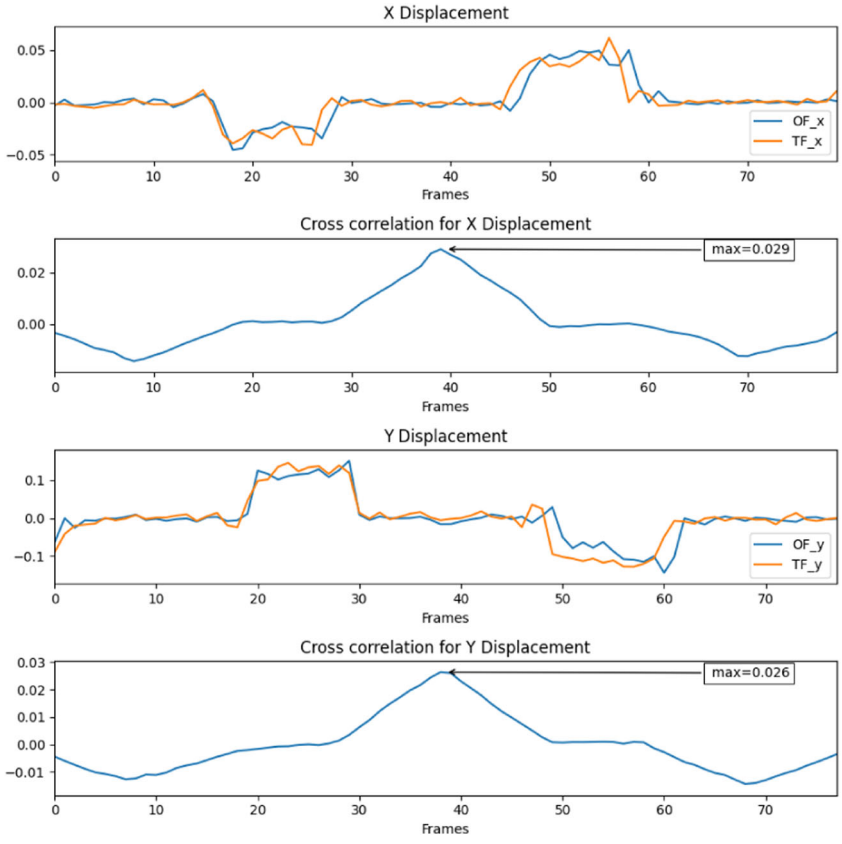

FIGURE A5 OF and TF signals at 1600 h. OF, optical flow; TF, thermal flow

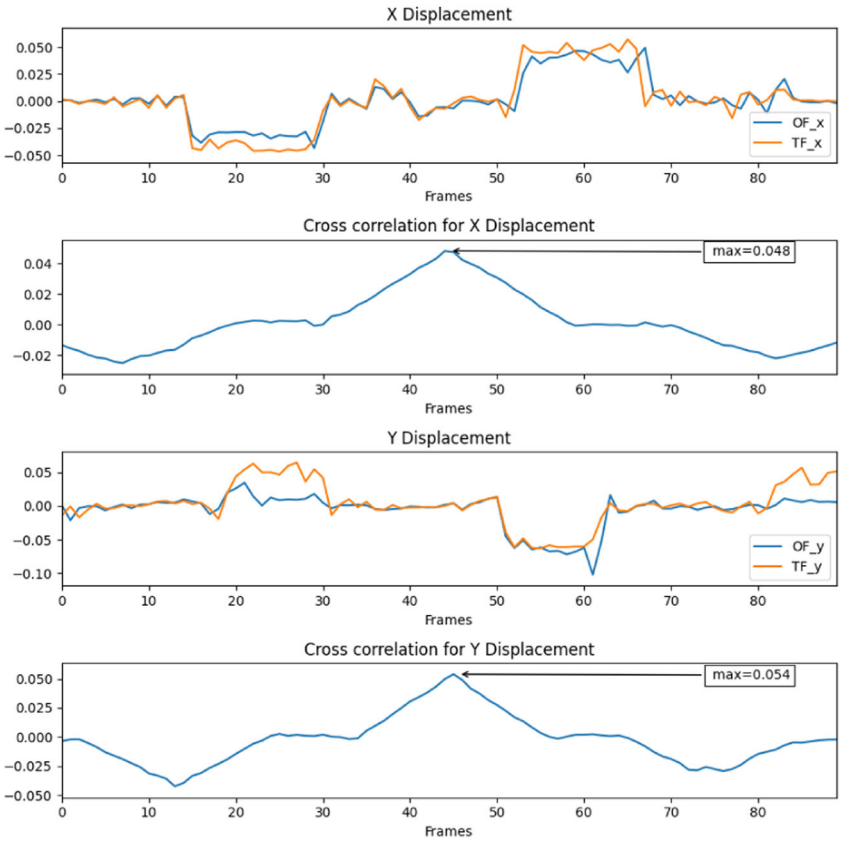

FIGURE A6 OF and TF signals at 1800 h. OF, optical flow; TF, thermal flow

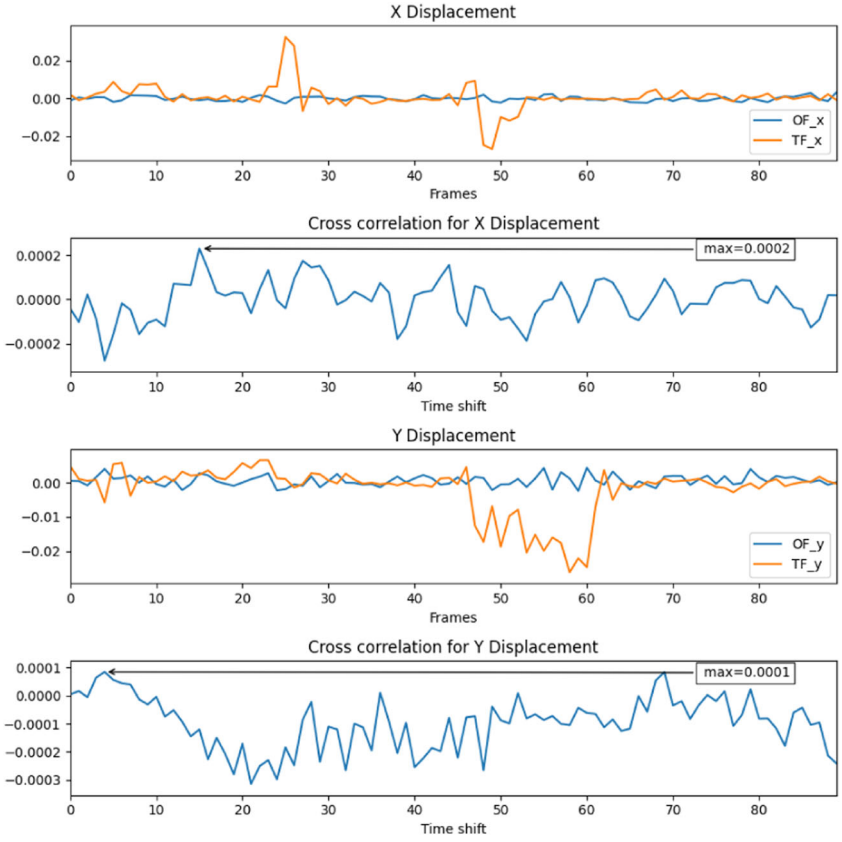

FIGURE A7 OF and TF signals at 2200 h. OF, optical flow; TF, thermal flow